SSC21-XIII-01

The AEPEX CubeSat Mission: Quantifying Energetic Particle Precipitation through Bremsstrahlung X-Ray Imaging

Grant D. Berland, Robert A. Marshall, Conner Martin, Deven Mhadgut, Joseph Buescher
Aerospace Engineering Sciences Department, University of Colorado Boulder
3775 Discovery Drive, Boulder, CO 80303; (303) 735-4900
Grant.Berland@colorado.edu

Richard A. Kohnert, Spencer Boyajian
Laboratory of Atmospheric and Space Physics
1234 Innovation Dr, Boulder, CO 80303; (303) 492-6412
Rick.Kohnert@lasp.colorado.edu

Christopher M. Cully
Physics & Astronomy Department, University of Calgary
2500 University Dr NW, Calgary, AB T2N 1N4, Canada; (403) 220-6088
cmcully@ucalgary.ca

Michael P. McCarthy
Earth and Space Sciences Department, University of Washington Seattle
4000 15th Ave NE, Seattle, WA 98195; (206) 685-2543
mccarthy@uw.edu

ABSTRACT

Fundamental gaps exist in the understanding and observation of energetic particle precipitation (EPP), a solar-terrestrial coupling mechanism that is vital for climatelogical modeling of the atmosphere and magnetosphere. The Atmospheric Effects of Precipitation through Energetic X-rays (AEPEX) mission is a 6U CubeSat that will measure energetic electron spectra and X-ray images in order to quantify the spatial scales and amount of energy input into the atmosphere, and therefore lost from the magnetosphere, via EPP. AEPEX includes two instruments; AEPEX's FIRE (Focused Investigations of Relativistic Electron) instrument (AFIRE), a TRL 9 electron detector previously flown on the FIREBIRD mission; and the Atmospheric X-ray Imaging Spectrometer (AXIS), an instrument being developed at CU Boulder that will take novel images and spectra of 50–300 keV X-ray photons. This work describes the AEPEX mission overview, the detailed design and operation of AXIS, and initial test and calibration results.

INTRODUCTION

The Atmospheric Effects of Precipitation through Energetic X-rays (AEPEX) is a 6U CubeSat mission that hosts two instruments to provide novel X-ray images of Earth to quantify outer radiation belt electron precipitation. Energetic particle precipitation (EPP) is a dynamic loss mechanism from the radiation belts that has various anthropological impacts, ranging from satellite damage to radio communication blackouts on Earth.[1,2] From a scientific perspective, EPP is responsible for depleting the flux of radiation belt energetic particles, and can serve as a proxy to study plasma wave activity in the magnetosphere via wave-particle scattering modes that deposit energetic particles into the atmosphere. EPP also has myriad atmospheric influences that are theorized to cause perturbative effects all the way down to ground level from excess ionization of the atmosphere to secondary particles produced by the high energy electrons.[3,4] EPP is therefore an important coupling mechanism between the Sun and Earth's magnetosphere and atmosphere.

The AEPEX mission aims to answer open science questions about EPP, including the spatial extent of EPP events and the total amount of energy deposited into the atmosphere from EPP, both of which are currently poorly constrained. These data are vital for the accurate and consistent modeling of Earth's magnetosphere and climate in whole-atmosphere models like WACCM-D.[5,6]

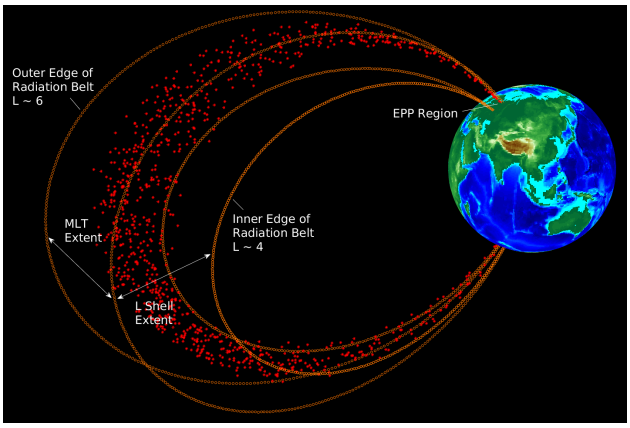

Figure 1: Geometry of Energetic Particle Precipitation and the Outer Radiation Belt

Energetic particle precipitation occurs when some fraction of the population of energetic electrons that are typically trapped in the magnetosphere enter the "loss cone," in particular the bounce loss cone (BLC), which is an area of the particle phase space in which electron bounce motion will reach a 100 km altitude towards the Earth. This altitude provides sufficient interaction between electrons and atmospheric neutrals such that the majority of that electron population is lost to the atmosphere. Various interactions occur in the magnetosphere that force electrons' into the BLC, including wave-particle interactions that cause pitch angle scattering which leads to diffusion of electrons into the BLC. Figure 1 shows the geometry of the outer radiation belts in their toroidal shape, which extends energetic electrons down to low Earth orbit (LEO) altitudes. L-shell is a generalized coordinate used in magnetospheric physics that is constant along a magnetic field line and maps approximately to latitude on the surface of the Earth, and magnetic local time (MLT) is a coordinate that maps to longitude.

Once they have entered the atmosphere, electrons lose energy through various scattering interactions. This is often modeled as a continuous energy loss that's proportional to the electron energy as the particles enter the collisional regime of the atmosphere that encapsulates a variety of physics interactions. One such high energy interaction is called Bremsstrahlung ("braking radiation") in which an energetic electron interacts with the nucleus of a neutral atom and greatly decelerates the electron. The heavier molecule is not accelerated significantly, and in order to conserve energy a photon is emitted (this is a simplified explanation using classical mechanics, see [7] and references therein for a more detailed explanation). Bremsstrahlung is a broadband emission where the resulting photon energy is a function of electron energy, the neutral species, and the interaction angle. Bremsstrahlung photons have the possibility of being emitted in any direction, including away from Earth and into space, and are within the X-ray regime, which makes Earth observations in X-ray a useful proxy for electron precipitation. Further, X-rays carry position and energy information in relatively straight lines from an EPP event to a spacecraft, and do not suffer from the same magnetic deflection that radio waves or charged particles might experience.

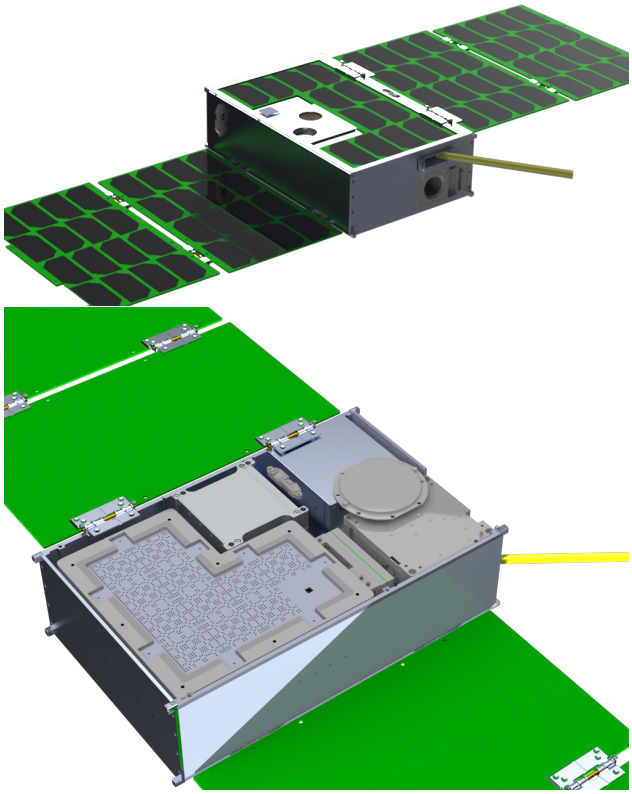

Figure 2: CAD Renderings of the AEPEX 6U CubeSat

Previous missions that have observed Earth in the X-ray band include NASA's Upper Atmosphere Research Satellite (UARS) which primarily imaged auroral precipitation from 3–100 keV using pinhole apertures.[8] The PIXIE instrument on the POLAR satellite measured 2–60 keV photons using multiple pinhole aperture detectors, and obtained the first global 2D images of electron precipitation.[9] Previous to that, collimated spectra within 50–500 keV were obtained from a spinning spacecraft, which resolved some spatial information.[10] From within the atmosphere, the Balloon Array for Radiation Belt Relativistic Electron Losses (BARREL) mission detected downward scattered X-rays with coarse spa-

tial resolution.[11]

AEPEX aims to provide comprehensive and novel X-ray images in the 50–300 keV band over the course of a year to perform a long-term study of EPP during a variety of geomagnetic conditions. The higher energy band also ensures that the mission will be imaging the more energetic particles and Bremsstrahlung radiation that occur from near- and ultra- relativistic electrons (sometimes referred to as energetic electron precipitation (EEP)), as opposed to auroral precipitation, which occurs via a different mechanism.

EPP is studied with various techniques, including Monte Carlo energetic particle simulations, such as the EPMC model and other radiation transport codes that use satellite measurements of energetic particle flux and spectra as upper boundary conditions, and propagate the energy deposition from electrons into the atmosphere using various numerical methods.[12,13] EPP is observed, either directly or indirectly, via satellite charged particle detectors and or through secondary effects of EPP. For instance, atmospheric plasma density measurements or atmospheric constituent measurements of odd nitric and odd hydrogen compounds (NO_x and HO_x) that are mainly produced by the excess ionization from EPP, can be inverted to estimate the total energy depostion of EPP that occurred in a spatially constrained region.[14,15] Each of these methods suffer from significant inaccuracies or limitations that perpetuate the uncertainty in various EPP parameterized inputs into other models. An inversion technique has been developed and is detailed in [16] to combine the electron spectra, X-ray images, and X-ray spectra to estimate the energy deposition and excess ionization of the atmosphere from EPP in order to answer our science questions and constrain EPP estimates for climatological modeling.[17] The work included here details the AEPEX mission operation, AXIS instrument development, and expected results from the mission.

AEPEX MISSION

The AEPEX mission consists of two instruments, AEPEX's FIRE (Focused Investigations of Relativistic Electron) instrument (AFIRE), a nearly build-to-print copy of the electron detectors used onboard the FIREBIRD mission,[18] and the Atmospheric X-ray Imaging Spectrometer (AXIS), being developed at CU Boulder. AFIRE points up the magnetic field line (in the anti-Earthwards direction) in order to measure the flux and spectra of precipitating and trapped electrons. AXIS faces Earthward (down the magnetic field line) in order to measure Bremsstrahlung photons that are produced from the precipitating electrons that are effectively backscattered anti-Earthwards (in the anti-BLC) towards the satellite. Through the novel X-ray spectra and images, and electron spectra and flux, the AEPEX mission aims to answer the following science questions:

Question 1: How much energy is deposited into the upper atmosphere through EPP? How is it related to geomagnetic storm and substorm activity?

Question 2: What is the spatial scale of precipitating regions during EPP events? What does this tell us about the total particle and energy flux removed from the radiation belts and deposited in the atmosphere?

See [19] for further reading and references therein on the AEPEX science goals.

Table 1: Mission Parameter Table

Parameter	Requirement	Reference Design
Altitude	400-600 km	500 km
Inclination	$\geq$70°	98°
Eccentricity	$\leq$0.02	0
Mass	$\leq$14 kg	11.7 kg CBE
Average Power	$\leq$37 W	26.5 W
Data	$\leq$210 MB/day	151 MB/day
Ground System	UHF/S-band	LASP UHF & S-band

AXIS is a novel X-ray imager being developed at CU Boulder which uses commercial-off-the-shelf Cadmium-Zinc-Telluride (CZT) detectors to extend measurements to 50–300 keV with 6.5% energy resolution, a modified uniformly redundant array (MURA) coded aperture optical system to increase signal-to-noise ratio (SNR) and provide 200 km spatial resolution,[20] and polyethylene-tungsten-tin graded-Z shielding to reduce the environmental radiation background on the detectors.

AFIRE is a set of two electron detectors; a near 2π detector and a collimated detector that fit within a 1/2U volume. See [18] for details on the original FIREBIRD electron detectors, which are considered TRL 9 instruments. Besides varying the electron energy bins and measurement cadence, minimal changes have been made to the detectors in order to integrate them into AEPEX.

AEPEX will operate both of these instruments polewards of 40 degrees latitude (i.e. above 40 degrees North and below 40 degrees South latitude) in a high-inclination orbit that provides coverage in magnetic local time, which is akin to longitude. A full science measurement (electron flux and spectra, X-ray images and spectra) will be taken every 10 sec-

onds as the spacecraft slews to maintain its optical axis along the magnetic field line.

AEPEX uses the ClydeSpace S-band radio and a UHF radio to transmit science and housekeeping data, respectively, to the Laboratory of Space and Atmospheric Physics (LASP) ground station. AEPEX's high power requirements necessitate four deployable and one body-mounted solar panel, with each of the former containing 16 cells for a total orbit-averaged power production of 26.5 W. The various components of AEPEX are shown in Figure 2, including the yellow "ruler" UHF antenna, the deployable and body-mounted solar panels, AFIRE on the top panel (two circular openings), and the Earthward-facing panel is removed to show AXIS. The large size and mass of AEPEX requires that a capable attitude determination and control system is employed: the Blue Canyon XACT system is chosen for AEPEX.

The relatively large size (6U) of AEPEX is necessary to accommodate the size and mass of the Redlen detectors, X-ray optics, and associated high-Z material shielding that reduces background radiation counts on the detectors. A size, weight, and power (SWaP) table is shown in Table 2, which details the two science instruments and bus volume, mass, and power draw.

Table 2: AEPEX SWaP Table

Item	Size	Weight	Power
AXIS	$\sim$ 4U	6.1 kg	18 W
AFIRE	$<$ 1/2U	0.3 kg	0.125 W
Bus	6U	6.6 kg	5 W

AEPEX will launch no earlier than Quarter 4 2022 on a ride-share launch opportunity into an orbit that will satisfy the missions minimum requirements. These orbital requirements are detailed in Table 1.

The AEPEX cubesat will be in a low Earth orbit (LEO) at high inclinations ($>70°$) with little to no eccentricity in order to maintain the detector-to-object imaging distance and ensure a consistent spatial resolution and field-of-view. As AEPEX is a rideshare opportunity, there is some uncertainty in the orbital characteristics, however AEPEX requires an orbit that will allow for sufficient downlink time for approximately 150 MB/day of data and 27 W orbit-averaged power. The nominal altitude of 500 km is the reference altitude used in the spatial resolution calculations.

ATMOSPHERIC X-RAY IMAGING SPECTROMETER (AXIS) DESIGN

The AXIS instrument consists of 12 Redlen, commercial-off-the-shelf (COTS) detectors, originally purposed for medical and security imaging. The number of detectors chosen for this mission is motivated by the relatively low amount of signal photons produced via Bremsstrahlung versus the abundant background due to the LEO space radiation environment. In order to produce the X-ray images that will be used to quantify the spatial scales of EPP, coded apertures are placed over the detectors in order to focus the X-ray photons. Coded apertures have their roots in astronomical imaging of point sources in the far-field, and adaptions have been made in order to image extended sources from a CubeSat platform.

A variety of issues arise adapting COTS components for CubeSats, including the significant amount of power needed to operate the 12 detectors, and in turn the significant amount of heat that needs to be removed from the instrument and radiated into space. Through the testing performed AXIS will advance to TRL 6 before launch.

The various aspects of the AXIS instrument are covered in detail in this section. Figure 4 shows a cross-section view of the instrument, showing the X-ray optics, collimators between detectors, two electronics boards, and the three layers of shielding.

Detectors

The detector selection is driven by the need to image the high energy regime of photons produced by the near- to ultra-relativistic electrons that produce Bremsstrahlung X-ray photons from the atmosphere. The Redlen M1770 Cadmium-Zinc-Telluride (CZT) solid state detectors, which were originally developed for medical and security X-ray imaging,[21] are chosen for the AXIS instrument. Out-of-the-box, the detectors have a 50–300 keV photon energy range with 6.5% energy resolution ($\sim$3 keV at 50 keV). The detector crystal is pixelated with 16 $\times$ 16 pixels such that each module has imaging capabilities, with each pixel having a maximum count rate of 230 counts/second/pixel, for a total of 60,000 counts/second/detector. Pixels are spaced at a 2.46 mm pitch.

The Redlen M1770 have heritage in low pressure environments via the EPEx balloon mission, which observed Bremsstrahlung X-rays from within the atmosphere. Modification are necessary to make these detectors space-compatible, including a stan-

dard conformal coating on the electronics boards. A bake-out tank test with residual gas analysis revealed the need to replace a silicone thermal pad that connects the ASICs and FPGA to the aluminum heat sink and mounting post. Additionally, the metal posts were drilled and tapped in order to precision mount the detectors within the instrument housing.

Background radiation and charged particles from the space environment will respond similarly to our expected signal, so shielding is developed in order to mitigate the background count rate.

Instrument Shielding and Housing

In order to protect against background radiation and charged particles depositing in the detectors and causing background signal, shielding has been developed for AXIS. The shielding also acts as a housing and mounting for the X-ray optics. The housing design chosen is graded-Z shielding, which mitigates background signals better than the same mass of any single homogeneous material.[22] Additionally, the "Z" here refers to the atomic number of the material.

Graded-Z shielding works by creating a gradient in material Z number, which is related to the stopping power efficiency of a given material. Low density materials are effective at stopping the large flux of low energy electrons that exist in an exponential energy distribution, but are effectively transparent to high energy electrons. There exists a tradeoff between collisional and radiative stopping power, in particular a high-Z material like tungsten has great stopping power against high energy electrons, but in turn produces Bremsstrahlung and/or X-ray fluorescence (XRF) photons. Tungsten's K-shell fluorescence lines are within 66–69 keV, which is within the AXIS detection range.[23] In order to reduce these effects, a lower Z material is placed within the tungsten shielding, in this case tin. Tin's highest energy fluorescence lines are at 27–29 keV, which is below the Redlen detection range.

A conformal coating will be applied on the inside of the tin material to mitigate tin whisker growth and to add a resistive layer in case of contact between the detector and inner shielding layer.

Although tungsten is one of the most effective radiation shields, the material itself is difficult to machine due to its high melting point and brittleness. A material chosen in place of pure tungsten is the Ecomass tungsten-nylon compound,[24] which suspends tungsten powder particles within the space-safe polyamide-12 epoxy compound. This material is readily machinable and is likely to burn up upon reentry, reducing the reentry debris risk posed by pure tungsten. The material thicknesses of polyethylene, tungsten-nylon, and tin are 15 mm, 6 mm, and 2.5 mm, respectively.

Table 3: AXIS Background Contributions

Source *(Model)*	**Contribution** [counts/second/detector]
Trapped and Precipitating Electrons *(AE-8 electron flux, Demeter energy spectra)*	∼10 – 100
Atmospherically Backscattered Electrons *(Marshall, et. al. 2018, EPMC Studies)*	∼1 – 10
Galactic Cosmic Rays *(Nymmik, et al. 1996, CREME86)*	∼100
Cosmic X-ray Background *(Hasinger, et. al. 1996, Gruber, et. al. 1999)*	∼10
Detector Background *(Lab testing)*	10 – 30

The 6 mm tungsten-nylon thickness is equivalent to approximately 3.5 mm of pure tungsten, based on the mass density of the Ecomass material material of 13 g/cm^3 (approximately that of lead) compared to the pure tungsten density of 19 g/cm^3. Figure 3 shows a prototype version of AXIS containing one sector of the instrument with graded-Z shielding surrounding 4 Redlen detectors with X-ray optics removed.

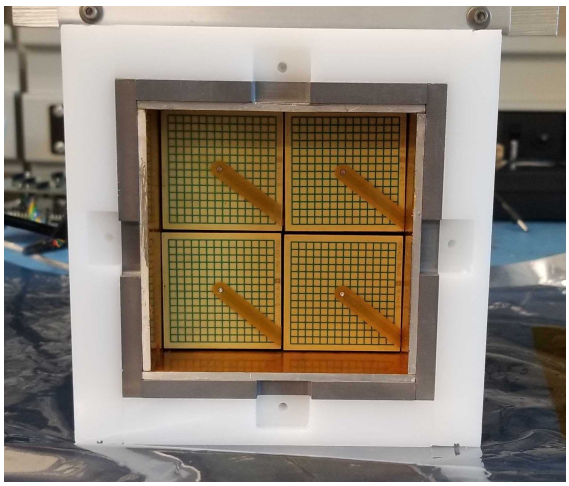

Figure 3: AXIS Instrument Prototype

The background sources considered in the simulations used to size the graded-Z layers include galactic cosmic rays (GCRs), cosmic X-ray background (CXB), trapped and precipitating electrons,

and atmospherically-backscattered electrons that do not precipitate and are within the instrument's field-of-view. Mass limitations are also considered in the shielding material and thickness optimization.

As the detectors consume approximately 1.1 W of power each, there is a significant challenge in removing heat from the detectors to the outside of the shielding and into the bus chassis. In order to ensure a low thermal noise environment for the detectors within their operation limits of 0–30°C, a "cold plate" is inserted between the shielding layers. This aluminum plate attaches directly to the detector posts and allows heat to be conducted directly to the bus rails, where it's then radiated out into space. This thin plate offers a fair compromise in that there's a small solid angle that background electrons would enter the instrument and the plate effectively maintains the detectors within their operational temperature limits. EM A beryllium window is included above the X-ray optics facing Earthwards in order to reject electrons that are within the field-of-view. This population is small relative to other background electron sources, but the field-of-view of the instrument offers the least protected portion of the instrument. Beryllium is chosen since the low-Z metal will most effectively mitigate electrons without creating Bremsstrahlung or XRF photons that might lead to spurious imaging results, and it is a common window material in high energy photon and particle instruments. This window thickness of 2 mm can block ∼300 keV electrons while providing over 97% photon transmission.

Imaging

One of the novel aspects of the AEPEX mission is the high-energy photon images that will be generated from EPP Bremsstrahlung. High energy photons, including gamma and X- rays, are difficult to image due to their penetrating nature and their proclivity to focus (scatter) only at oblique angles. X-rays in astronomical imaging are traditionally focused using Wolter-type optical mirrors that require large, high-Z (high mass) materials and have narrow energy bands. It is impractical to image X-rays in this method on a CubeSat platform due to the mass and volume constraints.

In order to form coherent images, the X-ray focusing technique chosen for the AXIS instrument is a coded aperture, simply explained as a pinhole imager with multiple pinholes that multiplex the object distribution onto the detector plane. The specific choice of open area elements must follow specified patterns such that the point-spread function (PSF) is, or is nearly, a perfect Dirac delta function. The process of coded aperture imaging can be described as a series of 2D convolutions:

$$I_{ij} = (A_{ij} \otimes \mathbf{O}_{ij}) + B \tag{1}$$

where A_{ij} is the aperture function (in this case a series of ones and zeros describing the transparent and opaque elements at position (i, j), respectively), $\mathbf{O}_{ij}$ is the object distribution, and therefore I_{ij} is the pattern projected onto the detector ($\otimes$ is the convolution operator). B is the mean of an additive Poisson noise process that does not get encoded into the detector pattern I_{ij} since the majority of the background counts come through the sides and back of the shielding. To complete the analogy, a pinhole imager's aperture function A_{ij} can be described as a narrow step function or sharply peaked 2D Gaussian that describes the size of the pinhole such that the convolution described in Equation 1 nearly exactly produces the original object distribution $\mathbf{O}_{ij}$.

However, unlike the pinhole imager, an additional step is needed to reconstruct the object distribution in the case of coded aperture imaging, as the pattern projected onto the detector I_{ij} is the encoding, or overlapping, of many pinhole images. In order to retrieve the image, the raw detector signal is convolved with the decoder function, in this case the anti-pattern of A_{ij} in the sense that $A_{ij} \otimes D_{ij} = \delta_{ij}$ where δ_{ij} is a Dirac delta centered on the image plane.

$$\tilde{\mathbf{O}}_{ij} = D_{ij} \otimes I_{ij} = \mathbf{O}_{ij} + D_{ij} \otimes B \tag{2}$$

where finally $\tilde{\mathbf{O}}_{ij}$ is the reproduction of the initial object distribution. $\tilde{\mathbf{O}}_{ij}$ is not equal to $\mathbf{O}_{ij}$ due to the encoded background noise $D_{ij} \otimes B$, but they approach each other in the case of no noise and perfect image encoding. This is the fundamental theory, with various caveats to coded aperture imaging described in [25]. The image reconstruction method implemented for this data is shown in Equation 3 which describes the real part of the Fourier-space multiplication (convolution) of the detector pattern and decoder array.

$$\tilde{\mathbf{O}}_{ij} = \mathcal{R}\left[\mathcal{F}^{-1}\left(\ \mathcal{F}(I_{ij}) * \mathcal{F}(D_{ij})\ \right)\right] \tag{3}$$

$\mathcal{F}$ and $\mathcal{F}^{-1}$ are the forward and inverse Fourier transform operators, respectively, and $\mathcal{R}$ is the real operator. Additionally, the detector pattern I_{ij} must be resampled to match an integer multiple of the size of D_{ij} in a process known as electronic focusing. Figure 5 shows on the left-hand side examples of I_{ij} for a point source and half-filled field-of-view

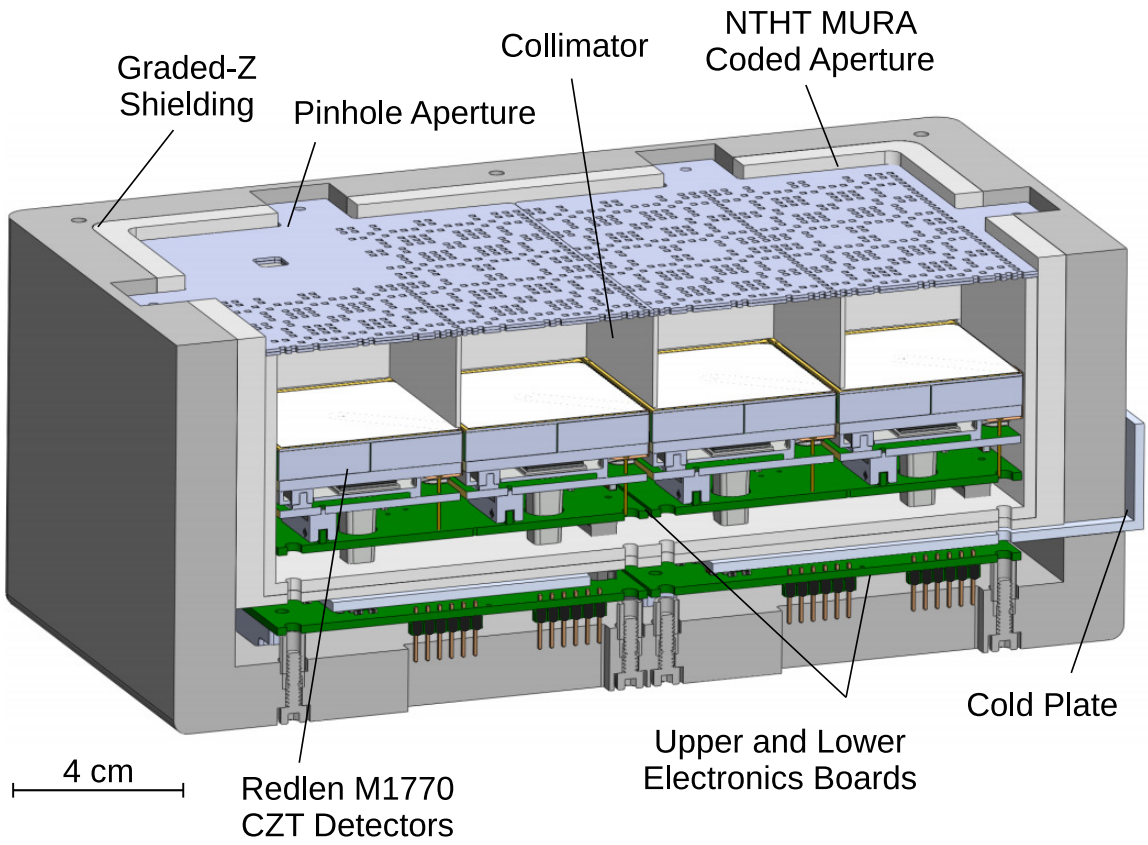

Figure 4: Cross Section View of the AXIS Instrument

source, respectively, with the right-hand side showing the image reconstructions $\tilde{\mathbf{O}}_{ij}$. Note the banding artifacts that develop as a result of the non-integer scaling between mask element size and detector pixel size, as well as the higher point source contrast in the final image reconstruction. The point source image has a Poisson SNR of approximately 40 while the half-filled source has an SNR of approximately 30. Decoder functions do not exist in general for arbitrary aperture functions, and of those that do exist, few have the desirable quality of having their PSF be a delta function. Of the existing masks, a Modified Uniformly Redundant Array (MURA) coded aperture[20] has the desired imaging qualities and is selected for AXIS. The base pattern selected has 17×17 elements with a 50% open area fraction. In particular, a No-Two-Holes-Touching (NTHT) variant is used which adds an opaque element between each row and column such that no solid element is left "floating" in the mask. This reduces the open area fraction of the mask to 12.5% and makes the mask 34×34 elements in dimension. This is done primarily for structural reasons so that the mask is secure during the vibrations induced during launch, although there is a slight advantage in imaging extended objects with a lower open area fraction.

The mask thickness is 1.25 mm, which is chosen via a tradeoff between the self-collimation effects of a thicker mask and the penetrative photon attenuation of thicker tungsten material. The equation in question that dictates the photon attenuation is shown in Equation 4,

$$f(x) = f_0 \; e^{-\mu(E)\rho\Delta x} \tag{4}$$

where $\mu(E)$ is the mass attenuation coefficient in the specific material at a given photon energy, in this case tungsten, ρ is the material density, Δx is the length that the photon transits within the material, and f_0 and $f(x)$ are the photon fluxes before attenuation by the materially and at point x in the material, respectively. In our case, μ is a function of energy and ρ is fixed from our material selection.

The tradeoff is then that the approximately lower half of energy bins (<50 – 160 keV) of AXIS provide low transparency (<1%), and the upper half

of energy bins (160 – >300 keV) gradually higher transparency, providing worse imaging quality (but better Poisson SNR), in the upper energy bins with no self-collimation of the 90° × 90° field-of-view.

The beryllium window that mitigates electron background in the field-of-view is 97% transparent on average to X-rays within 50–300 keV. The window therefore does not impede the X-ray signal significantly. Additionally, tungsten-nylon collimators are placed between each detector to limit cross-detector photon signals.

A pinhole aperture reference imager is included to provide one low-SNR image that will be downlinked separately. This reference image is used to constrain the image inversion and identify artifacts from the co-added image from the 11 other coded aperture imagers.

As an additional note, any X-ray within the field-of-view and in the 50–300 keV energy range should come primarily from EPP. There are no other major natural X-ray emitters in this energy band besides terrestrial gamma ray flashes (TGFs), which are more common at mid- to low- latitudes and are microsecond-scale events.[26] Earth's X-ray albedo over a range of energies is evaluated in [27] using SWIFT Earth-occulting measurements that are used to calculate Earth's reflectance to solar and CXB photons.

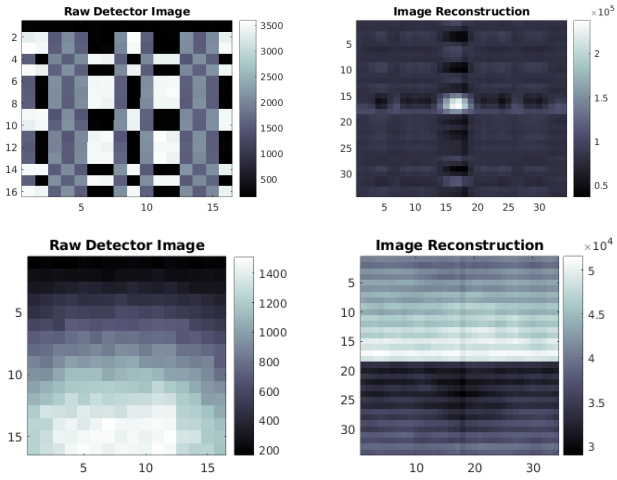

Figure 5: Example Coded Aperture Simulation Images

Electronics and Software

Two electronics boards are developed in order to process and handle the data generated by AXIS. The front-end electronics that perform the signal processing of photons are located within the Redlen M1770 detector modules. The detector modules interface immediately with an upper electronics board. The upper board provides the required power and voltages to the detectors for operation, and connects to the lower board which has a PIC32 microcontroller that stores the most recent X-ray image and performs the initial processing of the data. The microcontroller also handles the Redlen module signals, error codes, and produces and handles housekeeping data that tracks the state of the instrument. Housekeeping data includes the programmed voltages and detector temperatures and is also transmitted to the bus and downlinked.

The Redlen solid state detectors require a high voltage bias to be maintained across the CZT material in order to detect photons. A negative bias potential of 500V is applied to each detector, with associated electronics to support the supply and regulation of this voltage. The Redlen detector receives individual events, wherein an internal voltage threshold is passed and a photon arrival event is registered. This event is then output to the microcontroller where it's processed and converted into an energy level and the pixel address is logged. Average images that contain energy histograms are produced by each instrument sector by the contained detector every 10 seconds. Each sector, except for the sector with the pinhole detector, then sums the four detector images. These images are then 16 pixel × 16 pixel × 16 energy bins "data cubes" of multispectral images.

The two nominal sectors send their multispectral images to the bus C&DH via RS-422 where they are again summed to form single multispectral image. The third sector that has the pinhole aperture detector will send an image with three detectors and a reference pinhole image that's sent down separately. This describes the nominal science mode of AXIS where every 10 seconds a total of two images are produced, the summation of the 11 coded aperture detectors and the 1 pinhole reference image.

AXIS is posed as a state machine and has various other states, including a calibration mode which uses Redlen's built-in test pulser, and various other modes used for development and debugging.

A hot pixel detection algorithm is being developed in order to identify and correct for "hot" pixels, which do not have a strict count number definition in our case but are pixels that read out at a significant deviation above the rest of pixels and are caused by electronic malfunctions. The advantage yielded by summing multiple images to reduce the impact of background noise is lost when a hot pixel "washes out" the corresponding pixels from the 10

other detectors.

Additional capabilities include a heartbeat packet that is transmitted to the bus C&DH every 30 seconds in order to ensure proper operation of AXIS. The instrument also has the capability to re-calibrate the energy coefficients in-flight using the Redlen voltage test pulser.

Signal-to-Noise Ratio

In this section, we review various signal-to-noise ratios (SNRs) that have been used to quantify the AXIS predicted image quality. We start with the SNR from photons and background integrated spatially and over all energy bins in Equation 5, which we will refer to as the Poisson SNR, since we assume Poisson photon arrival statistics (yielding the $\sqrt{N}$ dependencies seen). We further break this SNR out into the Poisson SNR by energy bins, and we then address the spatial information with the MURA SNR formulation in Equation 6.

Equation 5 describes the SNR used to optimize the shielding thickness by reducing the background counts:

$$SNR^{Poisson} = \frac{N_{signal}\sqrt{n_{detector}\Delta t}}{\sqrt{N_{signal} + N_{background}}} \tag{5}$$

where N_{signal} is the rate of signal photon arrivals, $n_{detector}$ is the number of detector with co-added images, Δt is the imaging integration (exposure) time, and $N_{background}$ is the background count rate on the instrument due to space radiation background and intrinsic detector noise. From this equation, it can be seen that the SNR will go up as a square root with additional detectors or longer exposures.

Various other SNR formulations were used in the development of the X-ray optics, including the NTHT MURA SNR formulation referenced in [25]. This formulation is shown in Equation 6.

$$SNR_{ij}^{NTHT\ MURA} \propto \frac{\psi_{ij} N_{signal}\sqrt{n_{detector}\Delta t}}{\sqrt{N_{signal} + N_{background}}} \tag{6}$$

where $\psi_{ij} = \mathbf{O}_{ij}/N_{signal} \in [0,1]$ is an image extent parameter (note that the total counts and image distribution are related by $N_{signal} = \sum_{i,j} \mathbf{O}_{ij}$), $\mathbf{O}_{ij}$ is the object distribution from before, but more specifically it is the average number of photons per projected pixel grid as a function of spatial position (i,j) within the field-of-view. ψ_{ij} is therefore a measure of the compactness of the object.

This equation implies that compact objects are more readily imaged by a coded aperture system, and extended objects suffer a disadvantage. This can be thought of as a "spreading" of the SNR over the image. Nonetheless, the coded aperture provides SNR benefits in the EPP imaging scenario in all but the most extended object cases, in which case a filled FOV provides sufficient information in and of itself about the spatial extent of EPP.

An additional benefit of this imaging scenario is the dynamic motion of the spacecraft over the object that it is imaging. At approximately 7.5 km/s velocity and 10 second image exposures, a 1000 km $\times$ 1000 km field-of-view will have over 10 overlapping image segments. Similar to additional detectors or increased exposure time, this overlapping will increase the SNR by the square root of the number of overlapping image segments.

In order to determine signal photons versus background counts, we will assume that EPP X-ray object distributions are stationary on the timescales of an AEPEX flyover ($\sim$10's of seconds to a minute) and dynamic changes in the image are due to the encoded noise. This, in addition to the flux and spectra from AFIRE, will be used to estimate and tightly bound the X-ray photon flux within the image.

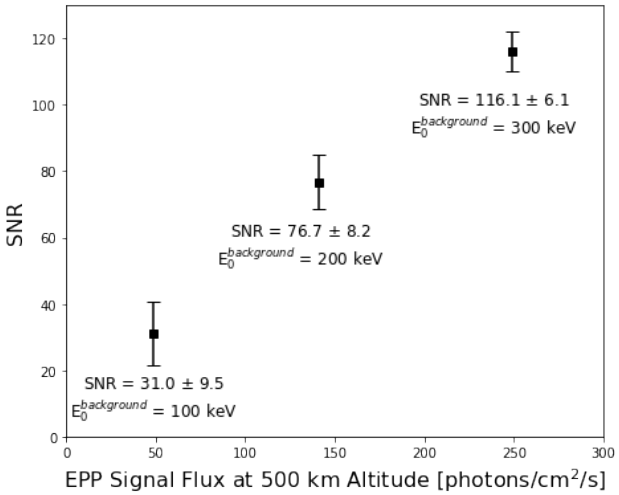

Figure 6: Poisson SNR of EPP Bremsstrahlung versus EPP Signal Flux

In order to convert the flux to signal counts, we assume that if a photon reaches 500 km altitude and hits the instrument, it is within the field-of-view. From EPMC modeling and photon raytracing, we find that the photon upward angular distribution is relatively uniform within the instrument's large field-of-view. We can then take the flux at AEPEX altitudes and convert it into detector counts from Equation 7.

$$N_{signal} = f_{EPP}\ A_{detector}\ \rho_{open}\ \eta_{QDE}\ \eta_{window} \tag{7}$$

where f_{EPP} is the signal flux in units of photons/cm^2/second, $A_{detector}$ is the detector area of 16 cm^2, ρ_{open} is the transparent (open) area fraction of $A_{detector}$ of 12.5%, η_{QDE} is the quantum detection efficiency of 60%, and η_{window} is the beryllium window transmission of 97%. This leads to the simple linear relationship of $N_{signal} = 1.2 \cdot f_{EPP}$ counts/second/detector where the signal count rate on the detectors are approximately the modeled flux at 500 km over an EPP event.

The pinhole imager SNR follows that stated in Equation 5 and has no spatial dependency on the object being imaged. This pinhole imager is implemented as a part of AXIS in order resolve extended object ambiguity from the rest of the imagers.

Figure 6 shows the Poisson SNR from Equation 5 evaluated at three nominal EPP conditions using 10^5 electrons/cm^2/s/str flux and a sine pitch angle distribution. An interesting note in this mission is that the very electrons that produce the EPP signal flux in the atmosphere also produce the unwanted background signal in the detectors. Due to this coupling, the abscissa of the plot fully describes both the expected signal and electron contribution to the background. The remainder of the background contributions are relatively constant within the region of operation of AEPEX, including the galactic cosmic ray (GCR) background, which yields the majority of the uncertainty in the error bars.

The background sources evaluated in the SNR calculation are noted in Table 3. Note the electron background is simulated in a 3D Monte Carlo simulation of the full instrument and spacecraft, and the GCR and CXB contributions are calculated theoretically using the parameterized flux and shielding attenuation. GCR secondaries are not considered in this analysis.

The Energetic Particle Monte Carlo (EPMC) model[12] was used to determine the signal generated from a typical EPP case. The simulation for the background electrons uses an exponential energy distributions with folding (mean) energy parameter E_0 from equation 8 of 100, 200, and 300 keV. These folding energies are chosen based on DEMETER observations from a range of nominal EPP events.[28]

The spatial and angular distribution of upward-propagating photons is also tracked, starting from an infinitesimally thin beam of electrons. We found when photons propagate upwards they transit the minimum distance through the attenuating atmosphere and therefore photons that are not propagating radially outwards from the Earth and collocated above an EPP event are filtered out.

$$f_1(E) = \frac{1}{E_0} e^{-E/E_0} \tag{8}$$

The backscattered photon energy distribution is found to be a combination of an exponential and power law energy distribution, which follows from the approximate $f(E)/E$ Bremsstrahlung spectra from input distribution $f(E)$, yielding Equation 8 divided by an additional factor of E, which drops off faster than an exponential in the high-energy tail. After photon propagation through the atmosphere, the behavior is similar to a power law within the detection range of AXIS, so a power law energy distribution of signal photons is used for simulation.

Energy Calibration

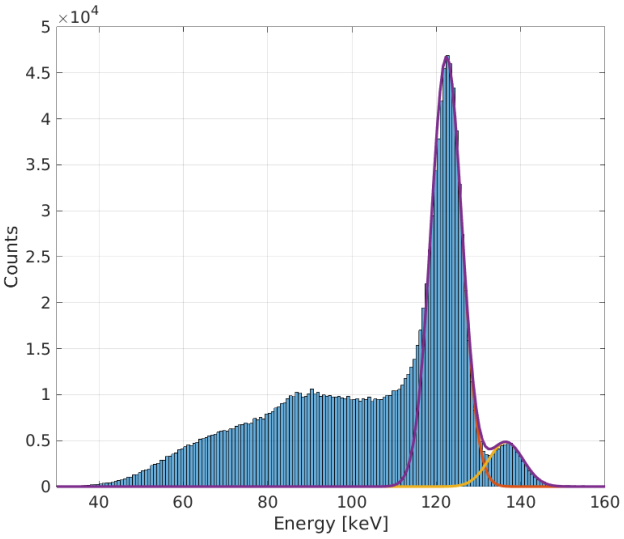

Figure 7: Cobalt-57 Spectra with a Gaussian Mixture Model Fit

A cobalt-57 radioactive source is used to calibrate the energy response of the detector to photons. Cobalt-57 emits photons predominately at 122 keV and 136 keV via beta capture. A small flux of beta particles are emitted in addition to photons, however they are quickly absorbed in air.[29] We use a Gaussian mixture model to fit the energy spectra and generate linear fit coefficients, i.e. the m and b coefficients of a $E = mD + b$ scaling per pixel, where D is the raw signal level and E is our output energy. Figure 7 shows the cobalt-57 source and the two fitted mixands. Note the Compton shoulder that develops at energies lower than the peak due to secondary electrons (not attributed to the primary electron-hole signal production) generated in

the detector material. This method is validated on one detector and has been automated for systematic calibration of the prototype and flight instruments

FUTURE TESTING

The following tests summarize the work remaining before the AXIS instrument is at TRL 6 and ready to integrate into the spacecraft:

- X-ray Imaging Tests
  - System point-spread function (PSF) characterization
  - Extended object imaging
  - Simulation of galactic X-ray sources for on-orbit performance evaluation
- Thermal Vacuum (TVAC) Tests
  - Thermal stress cycling
  - Thermal detector noise characterization
  - Source testing in vacuum
- Goddard Electron Beam Tests
  - GEANT4 verification and validation
  - Redlen detector electron response characterization

Imaging Testing

Imaging testing will be used to characterize the performance of AXIS and verify the image reconstruction method. The X-ray sources used for the energy calibration are concentrated in 0.25 inches within a 1 inch plastic disk, which is essentially a point source at significant enough distances from the detector. By bringing multiple point sources together, the system point-spread function can be determined along one axis by noting the point at which two point sources are indistinguishable from each other. Figure 8 shows a single disk source held 10 cm from the detector plane for a 30 second exposure, yielding a Poisson SNR of approximately 15.

By using long exposures and periodic motion of the point source within some angular region of the field-of-view, extended sources can be created in laboratory testing. Iterative methods can be used to increase the final image quallity, and an expectation maximization method is being developed to combine the information from the low-SNR pinhole image, the high-SNR coded aperture image, and the dynamic motion of the spacecraft that will overlap multiple images.

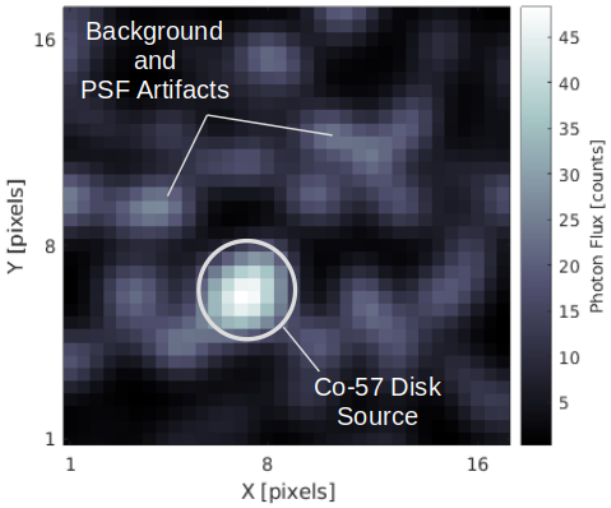

Figure 8: Cobalt-57 Disk Source Coded Aperture Image

There exist various galactic and extra-galactic hard X-ray sources that AXIS will be sensitive to. The AEPEX mission will leverage these non-terrestrial X-ray sources in order to assess the in-flight performance of the AXIS instrument. This procedure will be done periodically and compared to the simulated images in order to determine if there have been optical shifts during launch, energy calibration drifts, or other unforeseen degradation in the imaging performance.

Thermal Vacuum Testing

As noted in the Instrument Shielding and Housing section, the thermal performance of AXIS is critical to proper operation of the instrument. There exists some variation in thermal behavior based on the orbital parameters of AEPEX, so worst-case cold and worst-case hot situations are established and the design looks to accommodate those cases. The worst-case cold scenario is of little concern under full battery charging situations as the detectors act as their own 1 W heaters and can be duty cycled to maintain survival temperatures. However the worst-case hot scenario provides other challenges.

Similarly to infrared detectors, the Redlen detectors experience less thermal noise counts at cooler temperatures. We find that noise counts increase approximately linearly with temperature within the operating regime of 0-30°C, and then past a certain critical temperature, the noise counts increase exponentially. With this in mind, we aim to minimize the temperature of the Redlen detectors within the operational range. Modeling is compared with thermal

vacuum (TVAC) results in which a platen is driven to a specified temperature and the thermal behavior of the detectors is monitored. We find the thermal attachment to the bus in the prototype instrument case is a consistent 10°C cooler than the detectors, which is fed back into the thermal model. This behavior is expected of the flight instrument as well.

Goddard Electron Beam Testing

In order to validate and verify the GEANT4[30] shielding results, the prototype instrument will be tested in the NASA Goddard Radiation Effects Facility (REF) where they have electron and ion accelerators capable of energies up to 1.7 MeV. An additionally benefit of this testing is to characterize of the Redlen detectors to electrons. It has been assumed throughout simulation and analysis that photon and electron energy deposition in the CZT material is similar enough to bin similar energy photons and electrons into the same bin. The response to a monoenergetic electron beam is shown in Figure 9. GEANT4 modeling results of

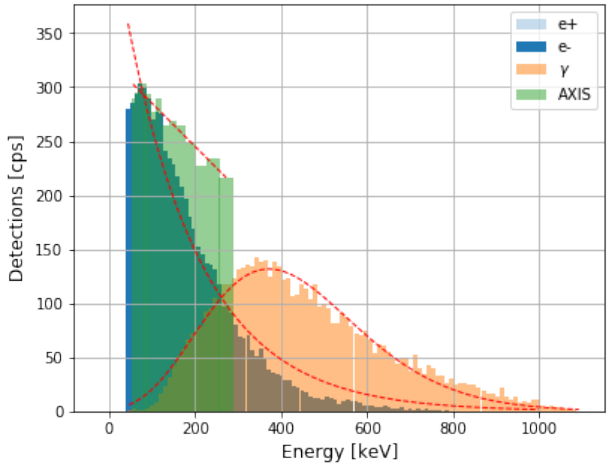

Figure 9: NASA Goddard Radiation Testing GEANT4 Modeling Results

penetrating electrons and Bremsstrahlung photons that deposit in the detectors are shown with high resolution, and the AXIS energy bins are shown in green. Electron spectra are fit with an exponential distribution and Bremsstrahlung photons are fit with a shifted gamma distribution.

DISCUSSION AND CONCLUSIONS

AEPEX will provide novel images and spectra of X-rays in the 50–300 keV band and electron flux and spectra generated from EPP in order to quantify the spatial scales and energy deposition of precipitation into the atmosphere over a variety of geomagnetic conditions over the 1 year nominal mission. An inversion method has been developed to estimate the precipitating flux and spectra of an EPP event that would generate the observed X-ray spectra and flux such that electron flux and spectra can be estimated. These data can be used as accurate inputs into magnetospheric and climatelogical modeling, and can also be used in scientific studies in its own right.

This dataset can be used in conjunction studies with other radiation belt-observing missions in order to provide synergistic studies of wave-particle interactions, atmospheric chemistry, and radiation belt dynamic behavior.

The novel instrument AXIS that's being developed at the University of Colorado Boulder will be the first miniaturized X-ray imager and spectrometer flown aboard a CubeSat and will pave the way for similar mission that observe Earth and space in the hard X-ray band with low size, weight, and power requirements.

Acknowledgements

This work is supported by NASA H-TIDeS grant #80NSSC19K0648. The authors would also like to thank the various engineers at LASP and CU Boulder students who contributed to this work, in particular Elliott Davis and Connor Myers for their early prototyping of the AXIS instrument. The authors would also like to thank Dr. Roberto Accorsi for his advice in coded aperture imaging techniques.

References

[1] Daniel N Baker. The occurrence of operational anomalies in spacecraft and their relationship to space weather. *IEEE Transactions on Plasma Science*, 28(6):2007–2016, 2000.

[2] RJ Redmon, DB Seaton, Robert Steenburgh, Jing He, and JV Rodriguez. September 2017's geoeffective space weather and impacts to Caribbean radio communications during hurricane response. *Space Weather*, 16(9):1190–1201, 2018.

[3] M Sinnhuber, H Nieder, and N Wieters. Energetic particle precipitation and the chemistry of the mesosphere/lower thermosphere. *Surveys in Geophysics*, 33(6):1281–1334, 2012.

[4] Esa Turunen, Pekka T Verronen, Annika Seppälä, Craig J Rodger, Mark A Clilverd, Johanna Tamminen, Carl-Fredrik Enell, and Thomas Ulich. Impact of different energies of precipitating particles on NOx generation in the middle and upper atmosphere during geomagnetic storms. *Journal of Atmospheric and Solar-Terrestrial Physics*, 71(10-11):1176–1189, 2009.

[5] Laura A Holt, Cora E Randall, Ethan D Peck, Daniel R Marsh, Anne K Smith, and V Lynn Harvey. The influence of major sudden stratospheric warming and elevated stratopause events on the effects of energetic particle precipitation in WACCM. *Journal of Geophysical Research: Atmospheres*, 118(20):11–636, 2013.

[6] ME Andersson, PT Verronen, DR Marsh, S-M Päivärinta, and JMC Plane. WACCM-D—Improved modeling of nitric acid and active chlorine during energetic particle precipitation. *Journal of Geophysical Research: Atmospheres*, 121(17):10–328, 2016.

[7] FV Bunkin and MV Fedorov. Bremsstrahlung in a strong radiation field. *Sov. Phys. JETP*, 22(4):844–847, 1966.

[8] JD Winningham, JR Sharber, RA Frahm, JL Burch, N Eaker, RK Black, VA Blevins, JP Andrews, J Rudzki, MJ Sablik, et al. The UARS particle environment monitor. *Journal of Geophysical Research: Atmospheres*, 98(D6):10649–10666, 1993.

[9] WL Imhof, KA Spear, JW Hamilton, BR Higgins, MJ Murphy, JG Pronko, RR Vondrak, DL McKenzie, CJ Rice, DJ Gorney, et al. The polar ionospheric X-ray imaging experiment (PIXIE). *Space Science Reviews*, 71(1):385–408, 1995.

[10] WL Imhof, GH Nakano, RG Johnson, and JB Reagan. Satellite observations of bremsstrahlung from widespread energetic electron precipitation events. *Journal of Geophysical Research*, 79(4):565–574, 1974.

[11] RM Millan, MP McCarthy, JG Sample, DM Smith, LD Thompson, DG McGaw, LA Woodger, JG Hewitt, MD Comess, KB Yando, et al. The balloon array for RBSP relativistic electron losses (BARREL). *Space Science Reviews*, 179(1-4):503–530, 2013.

[12] Nikolai G Lehtinen, Timothy F Bell, and Umran S Inan. Monte Carlo simulation of runaway MeV electron breakdown with application to red sprites and terrestrial gamma ray flashes. *Journal of Geophysical Research: Space Physics*, 104(A11):24699–24712, 1999.

[13] JM Wissing, H Nieder, OS Yakovchouk, and M Sinnhuber. Particle Precipitation: How the spectrum fit impacts atmospheric chemistry. *Journal of Atmospheric and Solar-Terrestrial Physics*, 149:191–206, 2016.

[14] Annika Seppälä, Pekka T Verronen, Mark A Clilverd, Cora E Randall, Johanna Tamminen, Viktoria Sofieva, Leif Backman, and Erkki Kyrölä. Arctic and Antarctic polar winter NOx and energetic particle precipitation in 2002–2006. *Geophysical research letters*, 34(12), 2007.

[15] CE Randall, V Lynn Harvey, DE Siskind, Jeff France, PF Bernath, CD Boone, and KA Walker. NOx descent in the Arctic middle atmosphere in early 2009. *Geophysical Research Letters*, 36(18), 2009.

[16] Wei Xu and Robert A Marshall. Characteristics of Energetic Electron Precipitation Estimated from Simulated Bremsstrahlung X-ray Distributions. *Journal of Geophysical Research: Space Physics*, 124(4):2831–2843, 2019.

[17] Wei Xu, Robert A Marshall, Xiaohua Fang, Esa Turunen, and Antti Kero. On the effects of bremsstrahlung radiation during energetic electron precipitation. *Geophysical Research Letters*, 45(2):1167–1176, 2018.

[18] Alexander B Crew, Harlan E Spence, J Bernard Blake, David M Klumpar, Brian A Larsen, T Paul O'Brien, Shane Driscoll, Matthew Handley, Jason Legere, Stephen Longworth, et al. First multipoint in situ observations of electron microbursts: Initial results from the NSF FIREBIRD II mission. *Journal of Geophysical Research: Space Physics*, 121(6):5272–5283, 2016.

[19] Robert A Marshall, Wei Xu, Thomas Woods, Christopher Cully, Allison Jaynes, Cora Randall, Daniel Baker, Michael McCarthy, Harlan E Spence, Grant Berland, et al. The AEPEX mission: Imaging energetic particle precipitation in the atmosphere through its bremsstrahlung X-ray signatures. *Advances in Space Research*, 66(1):66–82, 2020.

[20] Stephen R Gottesman and E Edward Fenimore. New family of binary arrays for coded aperture imaging. *Applied optics*, 28(20):4344–4352, 1989.

[21] K Iniewski. CZT sensors for Computed Tomography: from crystal growth to image quality. *Journal of Instrumentation*, 11(12):C12034, 2016.

[22] Wesley C Fan, Clifton R Drumm, Stanley B Roeske, and Gary J Scrivner. Shielding considerations for satellite microelectronics. *IEEE Transactions on nuclear science*, 43(6):2790–2796, 1996.

[23] WT Elam, BD Ravel, and JR Sieber. A new atomic database for X-ray spectroscopic calculations. *Radiation Physics and Chemistry*, 63(2):121–128, 2002.

[24] Robert R Durkee III. High-density composites replace lead. *Composites in Manufacturing*, 22(3):1–7, 2006.

[25] Roberto Accorsi, Francesca Gasparini, and Richard C Lanza. Optimal coded aperture patterns for improved SNR in nuclear medicine imaging. *Nuclear Instruments and Methods in Physics Research Section A: Accelerators, Spectrometers, Detectors and Associated Equipment*, 474(3):273–284, 2001.

[26] David M Smith, Liliana I Lopez, Robert P Lin, and Christopher P Barrington-Leigh. Terrestrial gamma-ray flashes observed up to 20 MeV. *Science*, 307(5712):1085–1088, 2005.

[27] E Churazov, S Sazonov, R Sunyaev, and M Revnivtsev. Earth X-ray albedo for cosmic X-ray background radiation in the 1–1000 keV band. *Monthly Notices of the Royal Astronomical Society*, 385(2):719–727, 2008.

[28] Ian C Whittaker, Rory J Gamble, Craig J Rodger, Mark A Clilverd, and Jean-André Sauvaud. Determining the spectra of radiation belt electron losses: Fitting DEMETER electron flux observations for typical and storm times. *Journal of Geophysical Research: Space Physics*, 118(12):7611–7623, 2013.

[29] D Delacroix, JP Guerre, P Leblanc, C Hickman, and Bill C Penney. Radionuclide and radiation protection data handbook, 2003.

[30] Sea Agostinelli, John Allison, K al Amako, John Apostolakis, H Araujo, P Arce, M Asai, D Axen, S Banerjee, G 2 Barrand, et al. GEANT4—a simulation toolkit. *Nuclear instruments and methods in physics research section A: Accelerators, Spectrometers, Detectors and Associated Equipment*, 506(3):250–303, 2003.